Proceedings of ASME Turbo Expo 2011
GT2011
June 6-10, 2011, Vancouver, British Columbia, Canada

GT2011-45541

A HIGH PERFORMANCE LOW PRESSURE RATIO TURBINE FOR ENGINE ELECTRIC TURBOCOMPOUNDING

Aman M.I. Mamat, Muhamad H. Padzillah, Alessandro Romagnoli and Ricardo F. Martinez-Botas

Mechanical Engineering Department
Imperial College London
United Kingdom

ABSTRACT

In order to enhance energy extraction from the exhaust gases of a highly boosted downsized engine, an electric turbo-compounding unit can be fitted downstream of the main turbocharger. The extra energy made available to the vehicle can be used to feed batteries which can supply energy to electric units like superchargers, start and stop systems or other electric units.

The current research focuses on the design of a turbine for a 1.0 litre gasoline engine which aims to reduce the CO_2 emissions of a "cost-effective, ultra-efficient gasoline engine in small and large family car segment". A 1-D engine simulation showed that a 3% improvement in brake specific fuel consumption (BSFC) can be expected with the use of an electric turbocompounding. However, the low pressure available to the exhaust gases expanded in the main turbocharger and the constant rotational speed required by the electric motor, motivated to design a new turbine which gives a high performance at lower pressures.

Accordingly, a new turbine design was developed to recover energy of discharged exhaust gases at low pressure ratios (1.05 - 1.3) and to drive a small electric generator with a maximum power output of 1.0 kW. The design operating conditions were fixed at 50,000 rpm with a pressure ratio of 1.1. Commercially available turbines are not suitable for this purpose due to the very low efficiencies experienced when operating in these pressure ranges.

The low pressure turbine design was carried out through a conventional non-dimensional mixed-flow turbine design method. The design procedure started with the establishment of 2-D configurations and was followed by the 3-D radial fibre blade design. A vane-less turbine volute was designed based on the knowledge of the rotor inlet flow direction and the magnitude of the absolute speed. The overall dimensions of the volute design were defined by the area-to-radius ratios at each respective volute circumferential azimuth angle. Subsequently, a comprehensive steady-state turbine performance analysis was performed by mean of Computational Fluid Dynamics (CFD) and it was found that a maximum of 76% of total-static efficiency, η_{t-s} can be achieved at design speed.

Keywords: Energy Recovery, Mixed-flow Turbine, Turbocompounding, Low Pressure, Performance Prediction, Flow Field

NOMENCLATURE

A	Area	[m^2]
b	Blade Height	[m]
$BMEP$	Brake Mean Effective Pressure	[bar]
$BSFC$	Brake Specific Fuel Consumption	[kg/kW/hr]
C	Absolute Flow Velocity	[m/s]
C_P	Specific Heat at Constant Pressure	[kJ/kg.K]
h	Specific Enthalpy	[kJ/kg]
K	Thermal Conductivity	
k	Specific Heat Ratio	
l	Length	[m]
$\dot{m}$	Mass Flow Rate	[kg/s]
M	Mach Number	
MFP	Mass Flow Parameter	$\left[\frac{kg}{s}\frac{K^{0.5}}{Pa}\right]$
P	Pressure	[Pa]
PR	Pressure Ratio	
R	Gas Constant	[kJ/kg.K]
r	Radius	[m]
S	Entropy	[kJ/kg.K]
T	Temperature	[K]
U	Rotor Velocity	[m/s]
u	Velocity	[m/s]
v	Exit Hub-to-shroud radius ratio	
VR	Velocity Ratio	
W	Relative Flow Velocity	[m/s]
$\dot{W}$	Power	[kW]
Z	Blade Number	
α	Absolute Flow Angle	

θ	Non-dimensional Flow rate	
β	Relative Flow Angle	
ε	Clearance	$[m]$
ϕ	Flow Coefficient	
γ	Cone Angle	
λ	Camber Angle	
Δ	Finite Change	
δ	Gradient	
η	Efficiency	
μ	Dynamic Viscosity	$[kg/m.s]$
ρ	Density	$[kg/m^3]$
σ	Entropy production Rate	$[kJ/kg.K.m^3.s]$
φ	Slip Factor	
Ψ	Blade Loading	

Subscript

0	Total/Stagnation Condition
1	Volute Inlet
2	Stator Inlet
3	Rotor Inlet
4	Rotor Exit
θ	Tangential Component
avg	Average
h	Hub
i	Incidence, vector component
j	Vector component
k	Vector component
l	Local Blade
is	Isentropic
m	Meridional Component
n	Point Number
opt	Optimum
P	Passage
R	Recirculation
r	Radial
rms	Root Mean Square
s	Shroud
t-s	Total-to-static
ψ	Azimuth Angle

Superscript

‘	Relative
—	Mean

1 INTRODUCTION

A highly boosted downsized engine is a current trend in the automotive industry in order to meet strict emission standards. The boosted downsized engine is almost always equipped with a turbocharger system. One such a system is a double stage compression option that includes a standard turbocharger and an electrically driven compressor. This electrically driven compressor is known as an electric booster. Usually, rechargeable battery storage supplies the electric power for the unit. Consequently, it would be advantageous to have an electric generator to meet its higher electrical power demand. A small turbine located downstream of the main turbocharger can be used to run this generator; the energy comes from the exhaust stream and thus leads to greater exhaust energy recovery. This arrangement is known as electric turbocompounding.

In this paper, the design and performance prediction of highly efficient lower pressure turbine for electric compounding will be discussed in detail.

2 LITERATURE REVIEW

Engine downsizing has been shown to be a significant solution in the reduction of carbon emission. Research carried out by Fraser et al. [1] found that by downsizing from a 2.0 L to a 1.2 L engine reduces CO_2 emissions by about 14.4 %. Furthermore, by extracting latent energy from the exhaust, fuel consumption can be reduced by 1% to 15% [1-5].

The exhaust energy recovery can be achieved by applying methods such as: an electric turbocharger or a secondary turbine. An electric turbocharger was investigated by Hopmann and Algrain [2] in their electric turbocompound unit recovering surplus energy from a turbocharger turbine. A similar method was also applied by Millo et al. [3] to generate about 7.6 kW of power at 130,000 rpm. This energy recovery from a single stage turbine was capable of increasing engine boost, but the compressor surged easily as the turbo speed increased at lower flow rates.

Another method to recover exhaust energy is to use two turbines arranged either in series or parallel [1; 4; 6]. In general, the main turbine is used to drive the turbocharger compressor. The second turbine, which operates at a lower pressure, drives the electric generator. Usually, the secondary turbine is coupled with the electric generator via a common shaft. Kapich reported that an Exhaust Power Recovery Gas Turbine (EPRGT), tested on a 6L diesel engine, could recover about 30 to 70 kW of energy at 30,000 rpm [4]. This EPRGT was operated at a higher mass flow rate (0.5 kg/s) and at a pressure ratio of 1.55. For a D segment car, such as the application of the current research, the exhaust mass flow rate is in the range of 0.02 kg/s to 0.06 kg/s. The available pressure at the exit of the main turbine is about 1.1 to 1.2 bar.

3 BACKGROUND AND OBJECTIVES

The function of a secondary turbine is to recover waste energy remaining in the gas stream after having passed through the main turbocharger turbine (HP turbine). As one can expect, the energy available is not large since most of the expansion occurs in the HP turbine and hence the second turbine has to be operated at lower pressure conditions.

In the current study, the secondary turbine is coupled to an electric machine for turbocompounding applications. The operational constraints for electric turbocompounding systems are mainly due to the electric machine which needs to run at an optimum constant speed over the entire engine driving cycle in order to work efficiently. In a heavily downsized engine such a requirement is particularly difficult to be achieved since at low engine rpm (below 1500 rpm), the low pressure ratio available (1.05-1.3) constraints the turbine to operate in a region where conventional turbine provide less than 40% efficiency. This is well shown in **Figure 1** where it is a given an example of the efficiency of a medium capacity turbine rotor which was designed to operate at 98,000 rpm and *PR* of 1.6; the figure shows the region of interest for turbocompounding superimposed to a conventional turbine map. From **Figure 1** it is apparent that a conventional turbine results in a poor turbine performance thus justifying the need for the design of a bespoke turbine for low pressure applications.

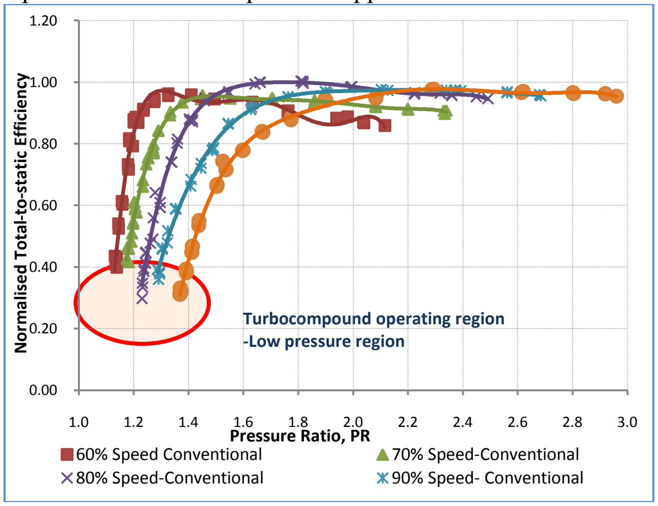

Figure 1: Mixed Flow turbine performance [16]c

For the particular application under study, the required operating conditions for the newly design turbine are given in **Table 1** below.

Table 1: Turbine Operating Requirement

Turbine Power	1 kW
Turbine expansion ratio	1.1
Blade rotational speed	50,000 rpm
Total inlet temperature	1100 K

In order to provide an insight into the benefits of adding the turbocompounding system to the engine, a simulation was also performed by using a commercial gas dynamics engine code (Ricardo Wave). A baseline model for the 1.0 litre gasoline engine under study was developed and validated against the experimental results. **Figure 2** shows the engine architecture and the location of the electric turbocompounding.

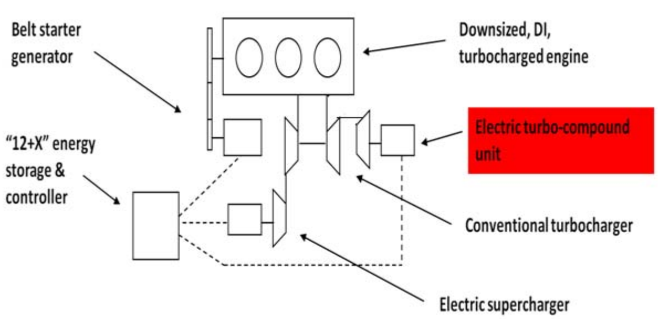

Figure 2: Engine Architecture

The model was initially ran for a range of engine speeds varying from 1000 rpm to 6000 rpm at steps of 500 rpm without the electric turbocompounding; the *BSFC* and *BMEP* of the engine were calculated. Then, the turbocompounding unit was included downstream of the main turbocharger. The model was run at similar operating ranges and the additional turbine power from the turbocompounding (≈ 1kW) was supplied directly to the crankshaft with the assumption of 100% mechanical efficiency. The turbocompounding was modelled as an isentropic nozzle with total-to-total efficiency of ≈ 75% and choking pressure ratio of ≈1.35 in order to emulate the operating conditions of the turbocompounding. The data were compared in **Table 2** and presented in **Figure 3** and **Figure 4**. The *BSFC* and the *BMEP* have been normalised to engine conditions at 2000 rpm.

Table 2: Impact of the turbocompound unit on Normalised BSFC and BMEP

Eng.speed [rpm]	BSFC		ΔBSFC [%]	BMEP		ΔBMEP [%]
	TBC	No TBC		TBC	No TBC	
6000	0.985	0.991	0.60	0.793	0.797	-0.52
5000	0.955	0.965	0.97	0.937	0.934	0.29
4000	0.901	0.912	1.11	0.978	0.972	0.56
3000	0.888	0.907	2.10	0.985	0.969	1.62
2000	0.929	0.952	2.47	0.992	0.969	2.30
1000	0.956	0.982	2.70	0.656	0.637	2.99

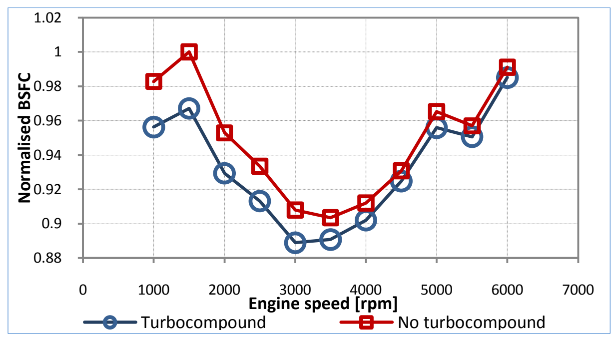

Figure 3: Impact of the electric turbocompound on BSFC

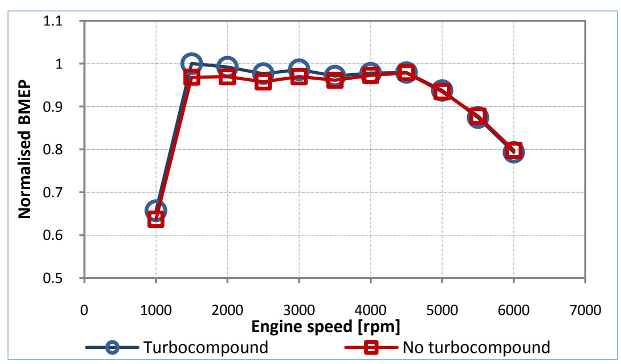

Figure 4: Impact of the electric turbocompound on BMEP

From **Figure 3** it can be seen that the addition of the turbocompounding unit is beneficial to the brake specific fuel consumption over the entire range of engine speeds. At lower engines rpm, a decrease of more than 2 percentage points could be calculated whereas as the engine speed increases (>3000 rpm) a decrease no greater than 1% can be obtained (**Table 2)**. The addition of the turbocompounding also proves to be beneficial in terms of *BMEP* for which an improvement of ≈2% to 3% could be estimated when the engine speed is in the range of 1000 rpm to 3000 rpm.

The outcomes of the 1-D simulation clearly show the benefit brought by the addition of an electric turbocompound unit in the engine thus justifying the need for a turbine which is able to operate efficiently at the required engine operating conditions.

In order to provide the reader with a better understanding of the analysis carried out within the paper, here below is provided a brief description of the main sections which will be discussed:

- ***Turbine design:*** a detailed description of the design procedure followed within the paper is given. The design method from the mean-line up to the full 3-D model is given for both the rotor and the volute;
- ***CFD analysis:*** the turbine performance investigation was carried out by using the single passage method and full-stage (volute-rotor) model via ANSYS 12.1 CFX;
- ***Flow field analysis:*** an evaluation over the flow distribution and the entropy generation is provided in this section.

4 TURBINE DESIGN OUTLINE

The turbine design started with non-dimensional mean-line loss model to define its 2-D rotor features. The mean line loss model is developed by applying turbine loss correlations for *passage loss*, *clearance flow loss*, *disc friction loss* and *incidence loss*. This method has been widely used by numerous researchers and has been proven to be a simple and reliable tool for preliminary design [7-9]. Several comparative researches showed that the mixed-flow turbine is better than the radial turbine [10-13]. Despite the many advantages of radial turbines, they have less geometrical flexibility due to the zero blade angle limitation which makes it difficult to achieve the optimum incidence angle. A mixed-flow turbine is a naturally back-swept wheel which offers two additional degrees of freedom, such as cone angle, γ and blade angle, β_{bl} [11] while still maintaining its structural stability [12]. This results in a greater flow capacity and in a reduction of the flow path curvature which effectively reduces the formation of secondary flow. This is one of the main advantages of a mixed flow turbine in respect to the radial counterpart [12].

With regards to the volute design, once the magnitude and the direction of absolute blade angle at the inlet to the rotor are identified, a suitable volute area ratio (*A/R*) can be defined. Hence a volute (either nozzled or nozzle-less) can be designed to provide the required rotor inlet conditions [14].

For the current application, the target total-to-static efficiency of the turbine was selected in the range of 65% to 75 %. Once the 1-D model of the turbine has been obtained, a 3-D Computational Fluid Dynamics (CFD) method can be employed in the design process to predict the turbine flow field and its performance [15].

4.1 Rotor Design

In this section is given a description of the design of the low pressure mixed flow turbine for electric turbocompounding. The non-dimensional design procedure is intended to determine the overall turbine configuration and its performance at design and off-design points. The operating requirements are defined in **Table 1** whereas in **Figure 5** the flow chart of the mean-line model for the rotor design is given.

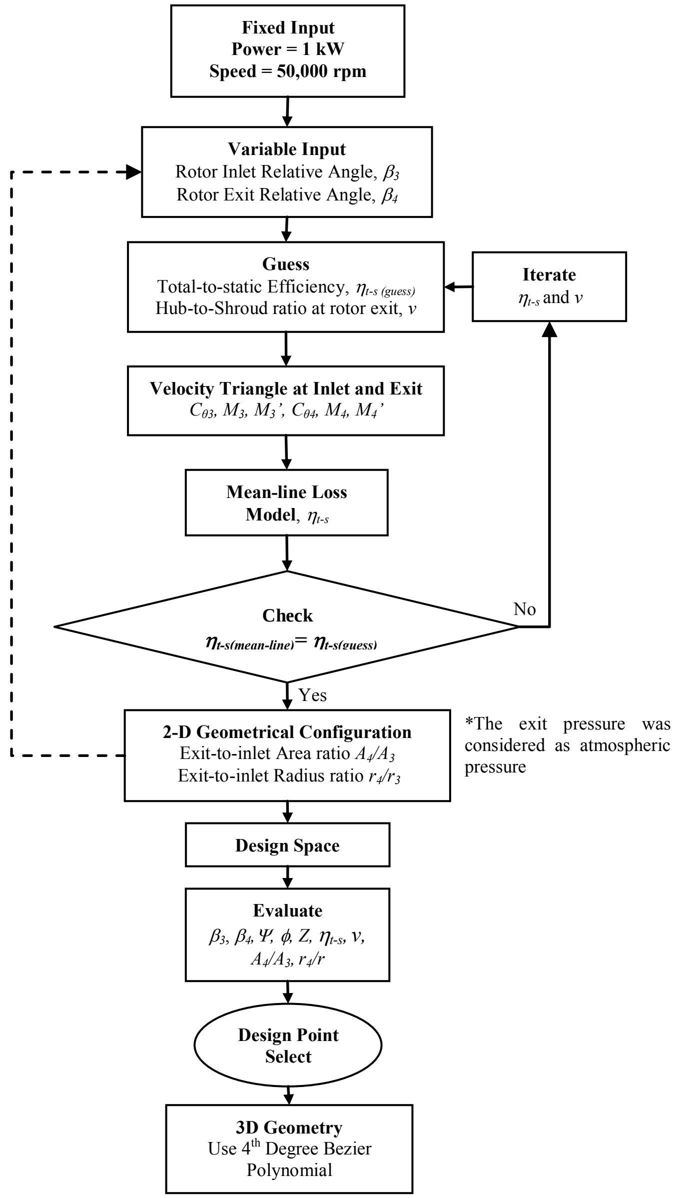

Figure 5: Rotor Design Mean-line Model

The design started by imposing the inlet relative flow angle, β_3 and exit relative flow angle, β_4. The cone angle, γ for the mixed-flow turbine was set at 70˚. Initially, the total-to-static efficiency, $\eta_{t\text{-}s}$ and leading edge hub-to-shroud ratio, v, were estimated. Then, the velocity triangle at the inlet and the exit to the rotor were solved in order to obtain the geometric results of the rotor. Afterwards, the mean-line loss model was applied to obtain the total-to-static efficiency, $\eta_{t\text{-}s}$. The iteration process continued until the values of efficiency converged. Then, the calculations were continued with different values of β_3 and β_4. Finally, the non-dimensional design modeling will produce a set of design space with possible combinations of β_3 and β_4. The design point was selected by assessing possible geometrical configurations that could give the optimum $\eta_{t\text{-}s}$. The selection procedure is presented in the next section.

Thereafter, the 3-D design configurations were defined by using the radial fibre blade design method which has a constant blade camber-line from hub to shroud. The blade camber-line was projected from the reference cylinder of radius, r_{ref}. The Bezier polynomial method was chosen to generate the blade geometry because of its simplicity and flexibility [11]. Finally a single passage 3-D CFD analysis was simulated by using ANSYS 12.1 commercial software. The Total-to-static efficiency, η_{t-s} was compared with the mean-line model. By mean of this comparison an optimum inlet absolute angle, α_3 is finally chosen and used as a reference for the volute design.

4.1.1 Mathematical Model and Design Selection

Several combinations of relative inlet and exit flow angles have been assessed during the design process. The correlation of the inlet absolute flow angle, α_3 and the inlet relative angle, β_3 is solved for a minimum inlet Mach number condition [16]; the solution for α_3 is given by Eq. (1).

$$tan\alpha_3 = \frac{sin\,\beta_3}{cos\,\beta_3 - 1} \tag{1}$$

Then, the non-dimensional rotor speed and power ratio, S_w can be determined by using Eqs. (2) to (4).

$$\frac{U_3}{a_{03}} = \left(\frac{1}{k-1}\right)\left(\frac{S_w}{\cos\beta_3}\right) \tag{2}$$

$$\frac{U_3}{a_{03}}\frac{C_{\theta 3}}{a_{03}} = \left(\frac{S_w}{k-1}\right) \tag{3}$$

$$S_w = \eta_{T-s}\left[1 - \frac{1}{(PR)^{\frac{k_{avg}-1}{k_{avg}}}}\right] = \frac{\dot{W}_{Required}}{\dot{m}h_{03}} \tag{4}$$

Thereafter, the correlation for blade loading, Ψ and flow coefficient, ϕ can be used as shown in Chen and Baines method [17]. **Figure 6** clearly shows that the optimum efficiency region occurs for flow coefficients in the range of 0.1 to 0.3 and blade loading coefficients between 0.7 and 1.1. A typical range of flow coefficients for a radial rotor is 0.25 to 0.38 which corresponds to an inlet absolute flow angle, α_3 in the range of 65˚ to 75˚ [17]. Another constraint for the rotor design is the number of blades of the rotor. The number of blades is determined by using the Glassman's relation [16] which has shown that the blade number decreases as the inlet relative flow angle, β_3 increases. A preliminary analysis on β_3 showed that a suitable number of blades would fall within 8 to 12. However it must be taken into account that a higher number of blades would result in a "blade crowding" at the exit to the rotor which might cause manufacturing issues. Because of this, the optimum flow coefficient and blade loading values were set at 0.27 and 0.78, respectively. These values correspond to a blade number of 9. Once the rotor inlet condition is fixed the rotor discharge configuration can then be developed. The design of the rotor discharge area was determined by correlating the non-dimensional mass flow rates at the inlet, θ_3 and at the exit, θ_4 to the rotor as given by Eqs. (5) to (7):

$$\frac{A_4}{A_3} = \frac{\theta_3\rho_{03}}{\theta_4\rho_{04}}\left(\frac{T_{03}}{T_{04}}\right)^{0.5} \tag{5}$$

$$\theta_3 = \cos\alpha_3 M_3\left(1 + \frac{k_{avg}-1}{2}{M_3}^2\right)^{-\left(\frac{(k_{avg}+1)}{2(k_{avg}-1)}\right)} \tag{6}$$

$$\theta_4 = M_4\left(1 + \frac{k_{avg}-1}{2}{M_4}^2\right)^{-\left(\frac{(k_{avg}+1)}{2(k_{avg}-1)}\right)} \tag{7}$$

From Eq. (7) the unknown parameter is M_4 which then was solved by imposing different values of β_4 to the exit velocity triangle. The variation of A_4/A_3 with β_4 is shown in **Figure 7**. From this figure it can be seen that A_4/A_3 increases in the range of 0.36 to 0.4 according to β_4. The typical value of A_4/A_3 for a conventional turbine is in the range of 0.75 to 1.1. **Table 3** shows a comparative study of conventional turbines and their design values. It is clear that the design point for a low pressure turbine is out of the conventional turbine range.

Figure 7 also shows the sensitivity of the total-to-static efficiency, η_{t-s} with the exit relative flow angle, β_4. The η_{t-s} was calculated by using a mean-line model that was applied by Bin Mamat and Martinez-Botas [9] and substituted into Eq. (4). The η_{t-s} value was solved for iteratively with the process shown in **Figure 5**. From **Figure 7**, it is apparent that the turbine efficiency, η_{t-s} increases as β_4 increases. Thus, β_4 value should be set as high as possible. However, the selection of exit relative flow angle, β_4 must consider other parameters such as the *hub-to-shroud ratio* at the trailing edge, v and the *inlet-to-exit radius ratio* $r_{4,s}/r_{3,rms}$.

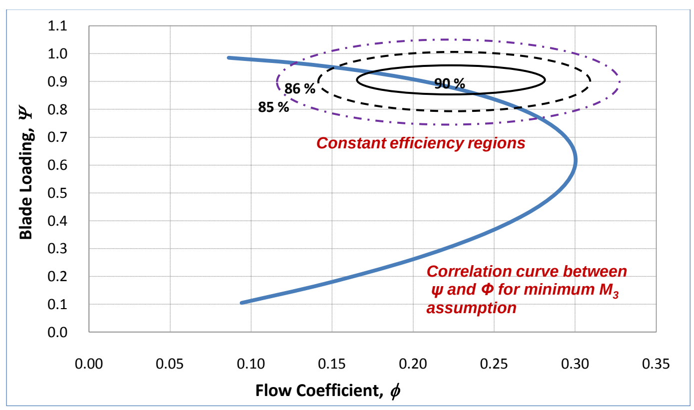

Figure 6: Superimposed of the calculated data to the empirical data of blade loading, Ψ and flow coefficient, ϕ

The final geometrical result was determined by using Eq. (8).

$$\frac{b_3}{r_3} = 0.5\left(\frac{r_{4,s}}{r_{3,rms}}\right)^2(1-v^2)\left(\frac{A_4}{A_3}\right) \tag{8}$$

The geometrical result is influenced by the choice of v. The ratio v not only influences the exit geometry, but also the rotor inlet blade's span. Thus, it correlates to Eqs. (4) to (6). The value of v was solved iteratively and finally, the geometrical configuration for the rotor was solved. A suitable geometrical configuration was selected as a compromise between aerodynamic performance and manufacturability. A large β_4 will increase the turbine swirl; thus it produces higher exit loss. Moreover, a large exit relative flow angle, β_4 creates a large turning of the fluid flow over a short blade chord. This increases the amount of secondary flow which contributes to larger entropy generation. Therefore, a larger value of β_4 is not suitable for the current turbine design due to the smaller operating range and the short blade chord length. This can be seen in **Figure 8** where the variation of β_4 is plotted against the exit-to-inlet and hub-to-shroud radius ratios. Most of the conventional turbines have the exit-to-inlet radius ratio, $r_{4,s}/r_{3,rms}$ greater than 0.7 [16].

Table 3: Conventional Turbine Area Ratio and Design Efficiency

	A_4/A_3	Design Efficiency	Design Speed (rpm)	PR
Caterpillar Medium Capacity Turbine	0.9	84 %	98,000	1.6
Small Capacity Turbine	0.8	72 %	160,000	2.0
ABB Turbine	1.1	80 %	60,000	2.0

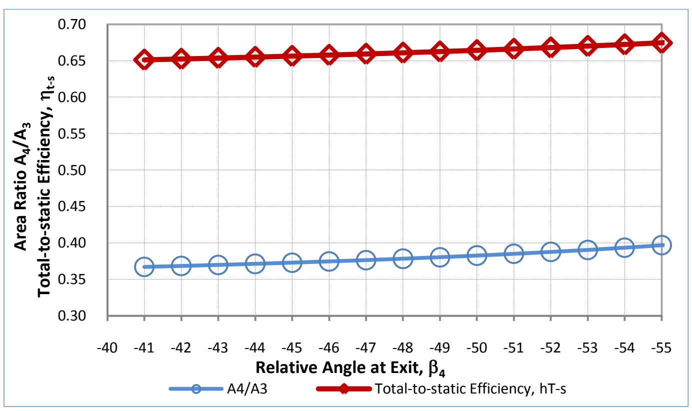

Figure 7: Relative Flow Angle variation to the Area Ratio and Total-to-static Efficiency, η_{t-s}

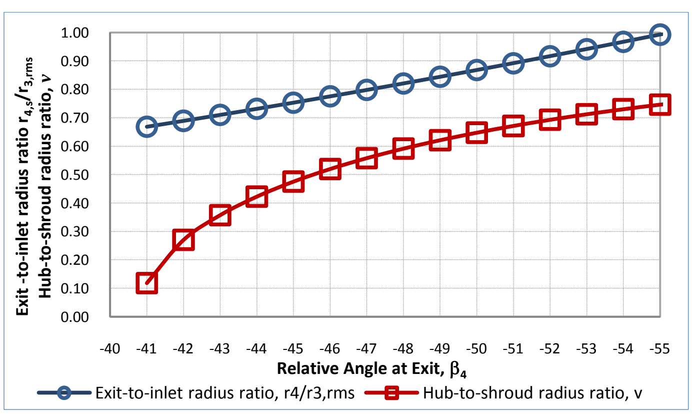

Figure 8: Relative Flow Angle variation to the Exit-to-inlet radius ratio and hub-to-shroud exit radius, *v*

The results of **Figure 8** show that the exit-to-inlet radius ratio ($r_{4,s}$ /$r_{3,rms}$) linearly increases as the β_4 increases and also that the ratio must not exceed 1.0. Thus, the selection of the β_4 value is also constrained by this criterion for optimum turbine geometrical configuration. A larger value of β_4 produces a better total-to-static efficiency, η_{t-s} (refer to **Figure 7**). However, this requires a larger value of $r_{4,s}/r_{3,rms}$ (> 0.8) which leads to a larger hub diameter with an increase in the inertia of the wheel. In contrast, a smaller value for $r_{4,s}/r_{3,rms}$ (< 0.7) increases the blade height and reduce total-to-static efficiency, η_{t-s}. Moreover, it causes the blades to be crowded together at the hub exit. A smaller radius hub with larger thickness reduces the exit area, thus limit the turbine operating range. However, smaller blades thickness reduces its strength capacity. Therefore, according to **Figure 8,** the optimum value for the exit relative flow angle, β_4 should be around -45˚, and $r_{4,s}/r_{3,rms}$ and v should have values of 0.75 and 0.5, respectively.

4.1.2 3-D Design Model

Once the hub and shroud geometrical results have been defined, a 4th degree Bezier polynomial curve was used to define seven meridional blade profiles starting from the hub up to the shroud. Thereafter, a single camber-line curve at the reference cylinder radius, r_{ref} was generated. Finally, the blade geometry was completed by using a radial fibre blade design method that projected the camber-line at the reference cylinder radius, r_{ref} to the meridional profiles. A completed 3-D turbine rotor is shown in **Figure 9**.

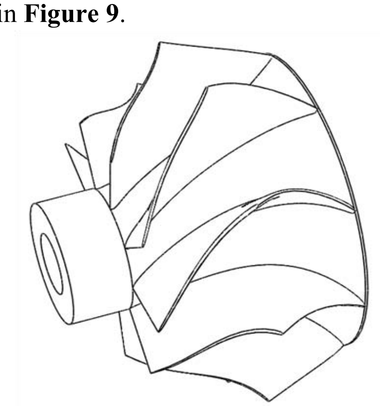

Figure 9: Mixed-flow turbine rotor: 3-D view

4.2 Volute Design

Prior to the design of the volute, an investigation into the turbine performance optimisation has been conducted by using a single passage CFD analysis. The commercial software CFD ANSYS 12.1 CFX was used in this investigation. The investigation was conducted by varying the absolute inlet flow angle, α_3 from 71.5˚ to 81˚. **Figure 10** shows the results of the CFD calculation where the inlet absolute angle, α_3 was plotted against η_{t-s} and the mass flow rate, $\dot{m}$. In this figure, the total-to-static efficiency, η_{t-s} and the mass flow rate, $\dot{m}$ have been normalised by the CFD results at the design point. The mass flow rate at the design point was reduced in order to maintain the design pressure ratio at 1.1. From **Figure 10**, it can also be seen that η_{t-s} increases as α_3 increases. Hence a new value for the absolute inlet flow angle, α_3 was set equal to 77˚.

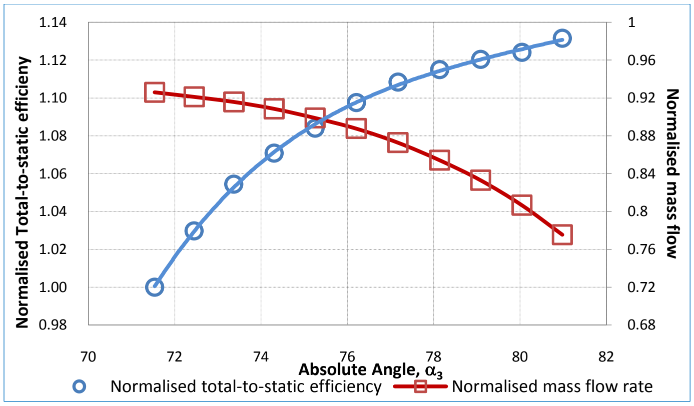

Figure 10: Absolute angle at inlet, α3 sensitivity

4.2.1 Non-dimensional Model

A volute is required to collect the working fluid and turn it towards the rotor while still maintaining a high tangential velocity. The volute design was carried out by assuming a uniform mass flow distribution around the periphery and mass flow recirculation ratio, $\dot{m}_R/\dot{m}$ to be in a range of 0 to 0.05 [18]. The correlation which informs the design of the volute is given in Eq. (9);

$$\left(\frac{A}{r}\right)_\psi = \frac{\dot{m}}{\rho_\psi (rC_\theta)_3}\left(1-\frac{\psi}{2\pi}\right)\left(\frac{\dot{m}_R}{\dot{m}}\right) \tag{9}$$

The non-dimensional mass flow rate was applied to define the area ratio (**Figure 11**) between each volute cross section as given in Eq. (10):

$$\frac{A_{\psi+\Delta\psi}}{A_\psi} = \frac{\theta_{\psi+\Delta\psi}}{\theta_\psi}\frac{P_{0\psi+\Delta\psi}}{P_{0\psi}} = \frac{(M\cos\alpha)_{\psi+\Delta\psi}}{(M\cos\alpha)_\psi}\left[\frac{1+\left(\frac{k_{avg}-1}{2}\right)M^2_{\psi+\Delta\psi}}{1+\left(\frac{k_{avg}-1}{2}\right)M^2_\psi}\right]^{\frac{-(k_{avg}+1)}{2(k_{avg}-1)}}\frac{P_{0\psi+\Delta\psi}}{P_{0\psi}} \tag{10}$$

By using Eq. (10), the volute configuration could be finally determined and the final results of this design process are shown in **Figure 12** where a 3-D view of the volute is given.

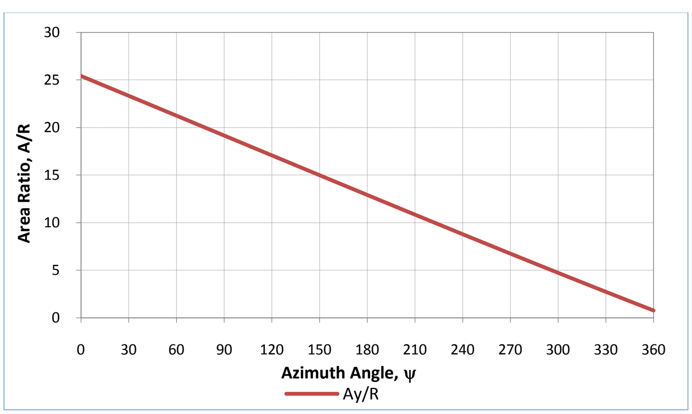

Figure 11: A_ψ/r distribution across the volute azimuth angle

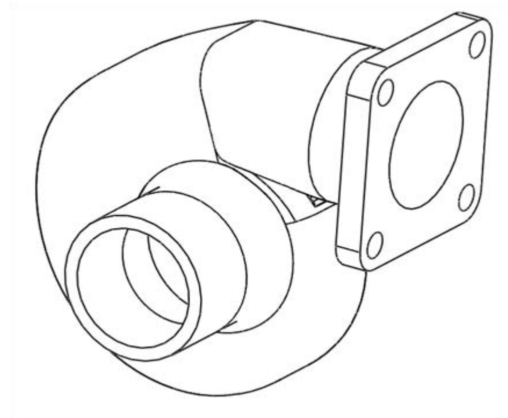

Figure 12: 3-D view of the volute design

It is worth noting that the volute cross section could not be designed following a conventional curved profile section. This is due to presence of the electric unit which would cause the turbine volute to interfere with the body of the electric unit. Hence a trapezoidal volute cross-section with a straight back was chosen and applied to the current design.

5 COMPUTATIONAL FLUID DYNAMICS

5.1 Numerical Technique

The main objective of CFD investigations is to analyse the performance and subsequently determine the flow field of the designed turbine [10; 19-21]. The employment of CFD during the design stage reduces the design lead time and costs. The CFD turbine performance investigation was carried out by using the single passage method and full-stage (volute-rotor) model via ANSYS 12.1 CFX.

The three dimensional Reynolds-Averaged Navier-Stokes equations (RANS) are solved using this technique. The k-ε turbulence model was used in this investigation. ANSYS CFX makes use of a scalable wall function which limits the y+[1] values used in the logarithmic formulation to 11.06 (intersection between the logarithmic region and the buffer region of the turbulent boundary layer) . This ensured that all mesh points which were outside the viscous sub-layers and all fine mesh inconsistencies were avoided [15]. Finally, the root mean square (RMS) residual value and maximum iteration steps for the solver control variables were set to 0.00001 and 1000 iterations, respectively.

5.2 Computational Model

The conventional validated CFD analysis that was applied by Copeland et al. [19] and Palfreyman and Martinez-Botas [10; 22] was used throughout this computational effort. For the full-stage model, the volute had been divided into three major sections to aid the meshing procedure using ICEM CFD. All the sections were blocked separately and then combined together in CFX Pre where the nodes in different sections were merged by using Domain Interface model that is available in the software.

[1] y+ is the non-dimensional distance from the wall to the nodes.

Table 4:Meshing nodes and elements values for single passage flow field study

Domain	Nodes	Elements
All Domain	1,228,306	1,172,688
Passage	1,072,221	1,028,544
Inlet	71,497	68,520
Outlet	84,588	78,624

The rotor passages were constructed by specifying the profile lines of the blades, hub and shroud. **Figure 13.a** and **13.b** show the generated meshes for full-stage and single-stage models. **Table 4** and **Table 5** show the total number of nodes and elements count for the models.

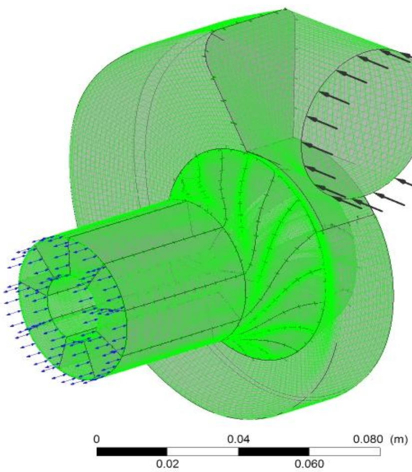

Figure 13.a: Full-stage meshing

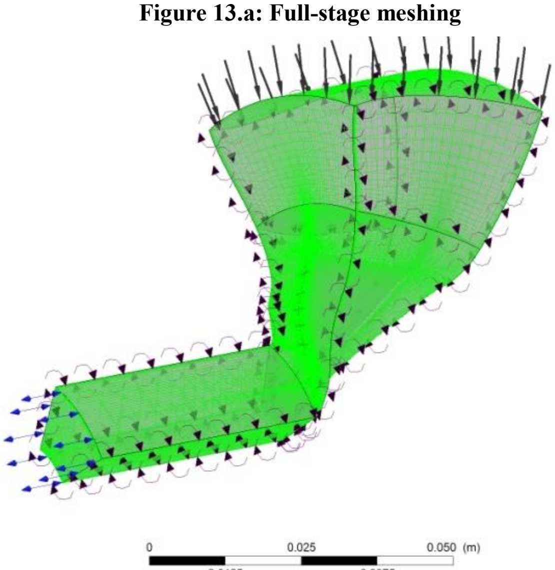

Figure 13.b: Full-stage meshing

Table 5: Meshing nodes and elements values for full-stage performance study

Domain	Nodes	Elements
All Domain	1,027,088	930,316
Rotor	820,116	747,900
Volute	73,342	64,480
Diffuser	133,650	117,936

5.3 Boundary Conditions

5.3.1 Inlet

Inlet boundary conditions (mass flow rate, flow direction, turbulence intensity and static temperature) were specified in the stationary frame of reference. The mass flow rate was obtained from the initial analysis done at design point. The flow direction of the rotor inlet for the single-passage simulation was assumed to consist of radial and tangential component only. The turbulence intensity was set equal to 5% which is similar to the value used by previous work done by Palfreyman and Martinez-Botas [19; 21]. The total temperature was set equal to 1100 K that corresponds to the operating conditions. The working fluid was assumed to be an ideal gas with the specific heat at constant pressure, C_P and specific heat ratio, k taken at the average value of $C_{P,avg}$ = 1533 J/kg and k_{avg} = 1.23.

A similar computational set up was also applied for the full-stage simulation with the flow entering normal to the volute inlet. The off-design performance was simulated for pressure ratios ranging from 1.04 to 1.35 by varying the inlet mass flow. The simulation was performed at 3 different operational speeds, 40,000 rpm, 50,000 rpm and 60,000 rpm that equals to 80%, 100% and 120% of the design speed.

5.3.2 Exit

An opening type boundary condition is was specified at the volute exit that referred to the stationary frame of reference. The opening static pressure and ambient temperature were applied (P_{exit}=100 kPa and T_{exit}=298.15 K) while the flow direction was assumed to be normal to the exit area.

5.4 Performance Results

The turbine performance was calculated by using a full stage CFD simulation. The performance characteristics are the Total-to-static efficiency, $\eta_{t\text{-}s}$ the Mass Flow Parameter, *MFP* the Velocity Ratio, *VR* the Pressure Ratio, *PR* and the Turbine Power, $\dot{W}$. The Total-to-static efficiency, $\eta_{t\text{-}s}$ and the Mass Flow Parameter, *MFP* have been normalised by the design values which are presented in **Table 6**.

Table 6: Performance Characteristics at design Point

Characteristics	Performance
Pressure ratio, *PR*	1.142
Velocity Ratio, *VR*	0.544
Total-to-static efficiency, $\eta_{t\text{-}s}$	0.721
Mass Flow Parameter	1.193

5.4.1 Turbine Efficiency

Figure 14 and **Figure 15** show the Total-to-static efficiency, $\eta_{t\text{-}s}$ as the velocity ratio, *VR* and the Pressure ratio, *PR* are varied. The peak efficiencies for all rotational speeds occur at *VR = 0.7*. This characteristic is similar to radial machines behaviour even though the peak efficiency, $\eta_{t\text{-}s}$ occurs at lower pressure ratios. This evidence is shown in **Figure 15** where the operating pressure ratio is in the range of

1.04 to 1.3. As compared with conventional turbines in **Figure 16**, it is apparent that the designed low pressure turbine is capable to operate in lower pressure region with higher efficiency. However, the operating region for the low pressure turbine is restricted since a significant drop in efficiency can be observed as we move outside this range.

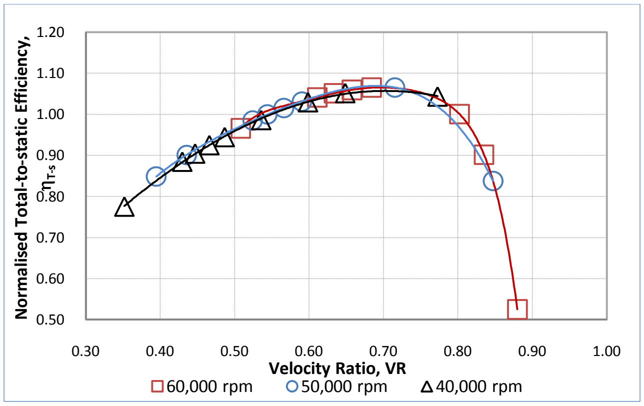

Figure 14: Normalised η_{t-s} vs Velocity Ratio, *VR*

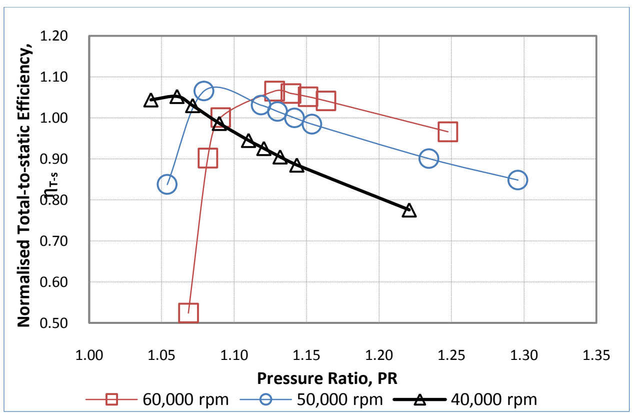

Figure 15: Normalised η_{t-s} vs Pressure Ratio, *PR*

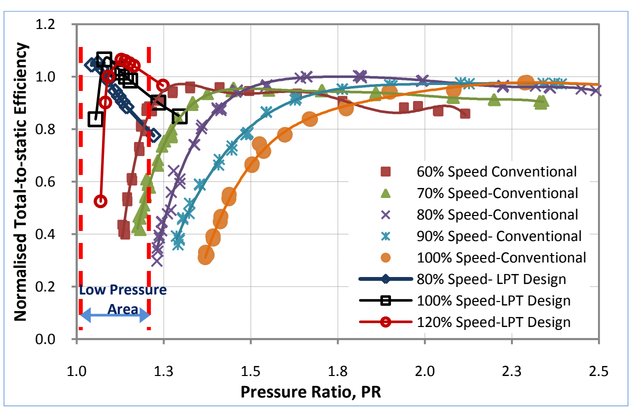

Figure 16: Comparison with Conventional Turbine

5.4.2 Mass Flow Characteristics and Turbine Power

The flow capacity of the turbine has been evaluated in terms of Mass flow parameter, *MFP* and plotted versus the Pressure ratio, *PR* as shown in **Figure 17**. From the figure, it can be seen that the flow capacity shows a trend which is in good agreement with other radial turbines for which the Mass Flow Parameter decreases as the rotational speed increases.

The CFD simulation was performed mainly near to the design point so that it would predict the turbine power variation in that region more precisely. This region is very important because it corresponds with the operational region of the turbine. **Figure 18** shows the turbine power predicted in the region which is in the range of 300 W to 3000 W.

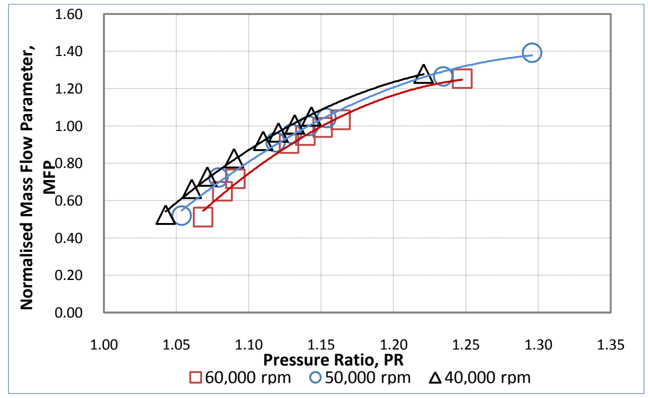

Figure 17:Normalised Mass Flow Parameter vs Pressure Ratio, *PR*

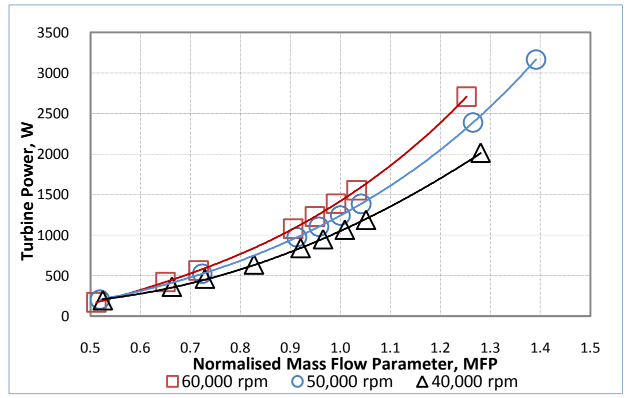

Figure 18: Turbine Power vs Normalised Mass Flow Parameter

5.5 Flow Field Analysis

The curl of the velocity, namely vorticity is a useful tool to visualise a highly distorted region in a particular flow field. **Figures 19.a-e** show the vorticity plot inside the rotor passage for different stream-wise locations. The contours are oriented such that the observer is looking downstream towards the trailing edge. The shroud is located at the top and the hub is located at the bottom. The pressure surface (PS) is located at the right of the plot whereas the suction surface (SS) is at the left as indicated explicitly in **Figure 19.a**. Rotation of the rotor is in the clockwise direction.

Leading Edge: The high accumulation of vorticity at the leading edge can be seen clearly at the suction surface and the shroud region. Movement of secondary flows up until approximately 80% span is from suction surface to pressure surface and the rest are moving from pressure to suction surface, creating counter clockwise direction across the plane. This counter clockwise movement is partly due to the Coriolis effect and the relative motion of the blade to the static wall. The localized vorticity in the vicinity of the suction surface is due to the flow impacting on this particular region since the blade is designed to have negative incidence across the leading edge span.

20% Chord: The localized region of vorticity continues to detach from suction surface and the intensity is now more pronounced towards the shroud. **Figure 19.b** clearly shows that there are two regions of high vorticity located next to each other. The vorticity region on the suction surface is believed to exist because of the tip leakage (feature A) where the other one (feature B) exist due to relative motion of the rotor and fixed shroud.

The secondary flow movement develops two regions of relatively large vortex structure as it evolves from the previous plane. One is located at the hub close to the pressure surface due to the high degree of turning in the meridional direction while the other one developed at the shroud close to the suction surface most probably due to interaction with the tip leakage flow. The existence of these vortices leads to additional radial velocity inside the flow passage which then continues to suppress the localized vorticity at the suction surface closer to the shroud and at the same time to detach any vorticity region from the suction surface. These vortices also cause one more horseshoe shape localized vorticity region (feature C) that develops near the pressure surface hub to migrate further to the suction surface.

40% Chord: In **Figure 19.c**, the secondary flow field continues to suppress the localized vorticity region close to the shroud and move them further up to 15% pitch. The high vorticity that has developed due to the relative motion of the wall (feature B) seems to migrate further in pitch-wise direction as compared to the one that existed due to tip leakage (feature A).

Another horseshoe shaped vorticity that was initially on its own at 20% chord close to pressure surface hub, has combined with the bigger vortex close to the suction surface and centred at 15% pitch at the shroud in this stream-wise plane.

80% Chord: In **Figure 19.d,** the movement of secondary flow is still predominately in the tangential direction which is from pressure to suction surface. The region of high vorticity has moved further to the centre of the passage but is still constrained near to the shroud wall. Moreover, the localized vorticity has migrated downward to 70% span, in the centre of the passage (feature C)

Trailing Edge: As can be seen in **Figure 19.e**, the relative flow velocity exited the turbine with a high tangential velocity and the radial component can be neglected. The localized vorticity near the shroud that is caused by the relative motion of the shroud wall (feature B) has migrated further towards the pressure surface where the vorticity created by tip leakage (feature A) stays in the middle of the passage close to the shroud. The localized velocity finally stays at 70% span but moves further towards the pressure surface (feature C).

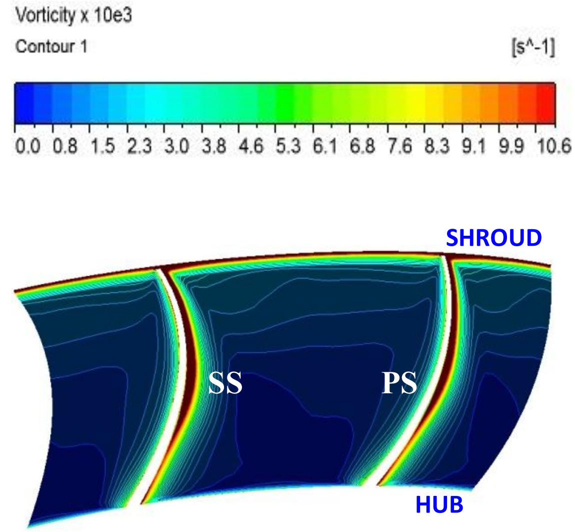

Figure 19.a: Leading Edge

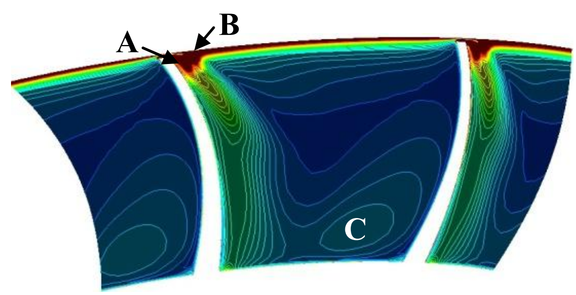

Figure 19.b: 20% Chord

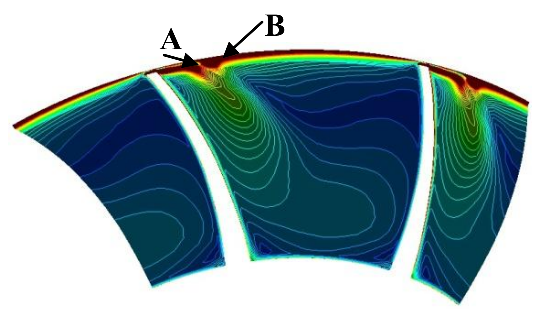

Figure 19.c: 40% Chord

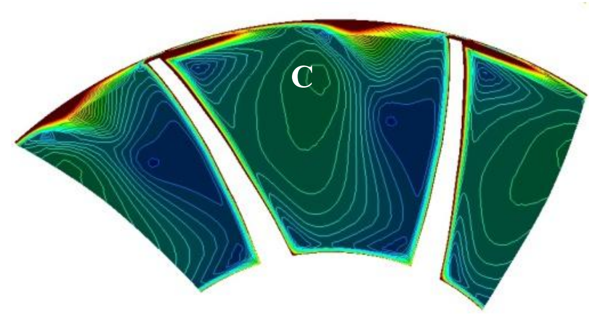

Figure 19.d: 80% Chord

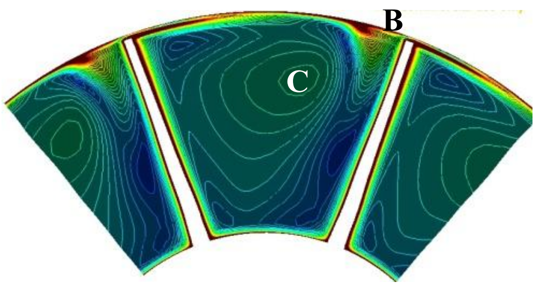

Figure 19.e: Trailing Edge

Figure 19.a-e: Vorticity contour plot

5.4.1 Entropy Generation Contour

The loss production in the flow field can be highlighted by the rates of entropy generation per unit volume per unit time. The equation for entropy generation rate, taking into account the turbulent fluctuation is provided by Moore and Moore [23] and is presented in Eq. (11):

$$\bar{T}\bar{\sigma} = \frac{K_{eff}}{\bar{T}}\left(\frac{\partial \bar{T}}{\partial x_j}\right) + \mu_{eff}\left(\frac{\partial \overline{u_i}}{\partial x_j} + \frac{\partial \overline{u_j}}{\partial x_i}\right)\frac{\partial \overline{u_i}}{\partial x_j} \tag{11}$$

This simple equation is based on a few underlying assumptions that the effect of turbulent pressure and that gradients of density in the flow direction are negligible. The rate of production of turbulent kinetic energy is also assumed to be equal to the rate of its dissipation to produce entropy, and similarly, the rate of production of temperature fluctuations is assumed to be equal to their rate of dissipation [22].

In the current work, the turbine is assumed to be an adiabatic turbine thus the first equation on the right hand side of Eq. (11) goes to zero, and the entropy generation rate has a one-to-one relationship with the components of velocity gradient. **Figure 20** shows the contour plot of each component of velocity gradient at 50% chord showing that most of the entropy generation in the rotor passage originates at the tip clearance region.

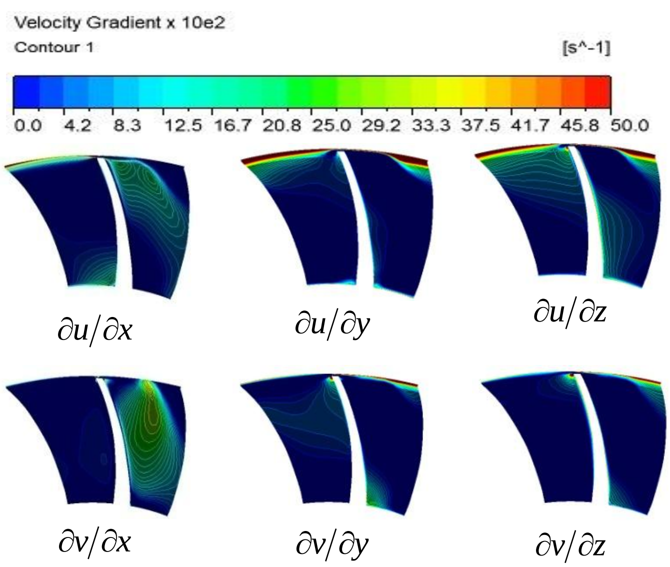

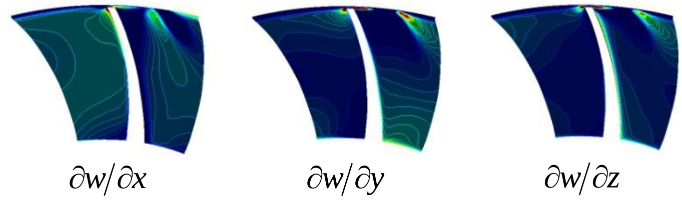

Figure 20: Velocity gradient at 50% Chord contour plot

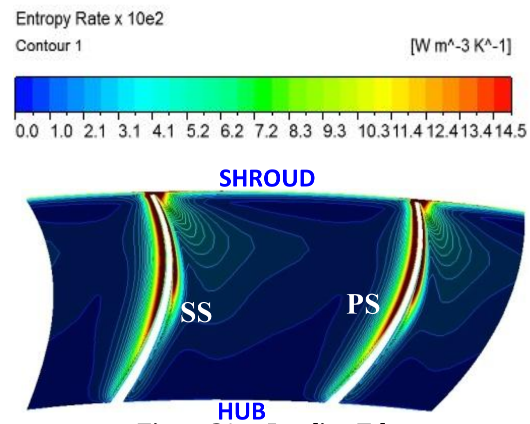

Figure 21.a: Leading Edge

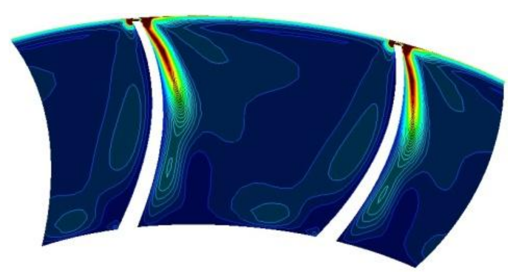

Figure 21.b: 20% Chord

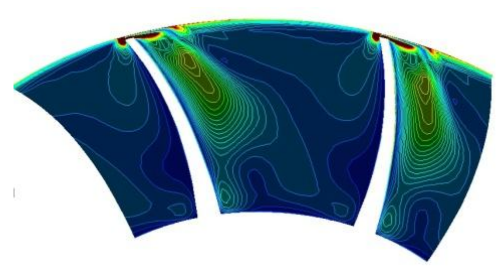

Figure 21.c: 40% Chord

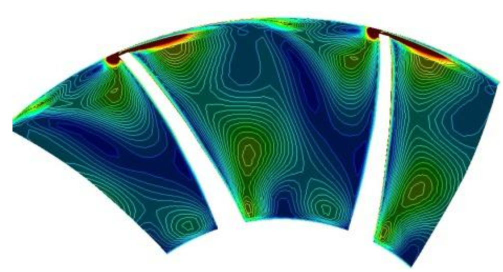

Figure 21.d: 80% Chord

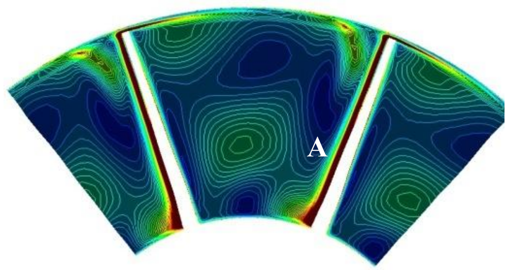

Figure 21.e: Trailing Edge

Figure 21 a - e: Entropy Generation contour plot

Entropy generation plot at each chord length enables visualization of regions with high losses inside the rotor passage and its propagation from the leading edge downstream towards the trailing edge. The contour plot shows similar behaviour to that of the vorticity plot. **Figures 21.a** to **21.e** indicate that the highest rate of entropy generation is located in the tip clearance region. However, the tip clearance loss contributes only 3 to 5 % of total rotor losses [24] where a bigger tip clearance increases the tip clearance loss. The passage loss is therefore best represented by the entropy generation regions. The biggest rotor loss is the passage loss and it combines the effects of the secondary flow and fluid friction [16]. A large entropy generation in the middle of the passage corresponds to the large secondary flow. Meanwhile, large entropy generation on the wall of the rotor hub and blade surfaces correlates to the magnitude of wall shear stress.

At the leading edge, a high entropy generation region localises in the presence of blade surface and develops towards the hub at the pressure surface. This is probably due to the rapid acceleration and deceleration of the flow impacting the leading edge. Furthermore, the high region of entropy generation close to the blade surfaces could also be influenced by the interaction with wakes from upstream blade rows.

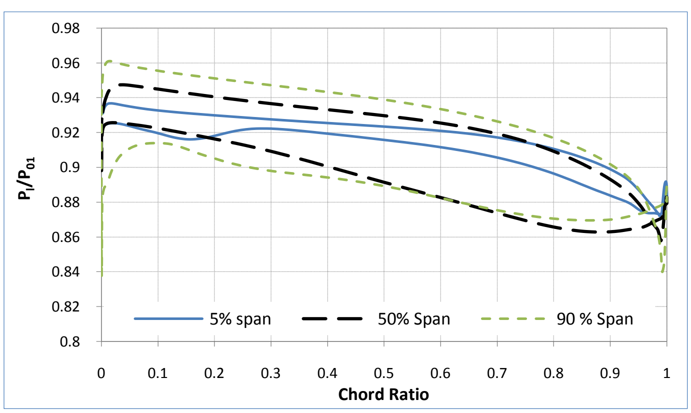

Figure 22: Blade loading at various blade spans along the chord

Starting from 20% chord to the trailing edge, the relative motion of rotor and stationary shroud has become another main contributor to the high entropy generation region and is located next to the tip leakage high loss region. From 20% to 60% chord, the entropy generation concentrates on the suction surface rather than to the pressure surface. This is possibly caused by the acceleration of the relative flow that increases the velocity gradient and rapid increment of wall shear stress on the suction surface as compared to the pressure surface. However, as the flow moves further downstream, the region of localized entropy generation floats away from suction surface towards the passage centre. On the other hand, it is believed that the stream-wise plane at the trailing edge in **Figure 21.e** indicates a high entropy generation region at the pressure surface that covers the whole span (feature A) due to wakes that develop on the pressure surface in the inducer section.

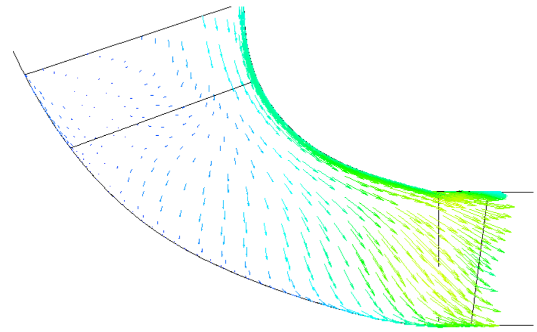

Figure 23.a: Pressure Surface

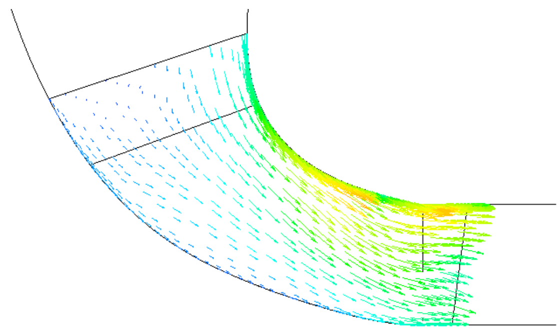

Figure 23.b: 50% Pitch

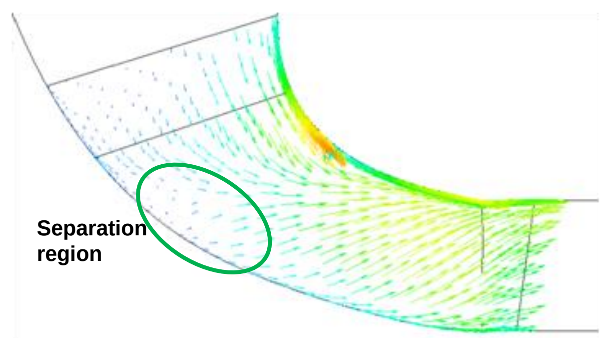

Figure 23.c: Suction Surface

5.4.2 Blade Loading

In **Figure 22**, the blade loading is represented for different blades-spans and it is obtained by normalizing the local static pressure, P_l with the total inlet pressure, P_{01} at different locations along the blade chord. The figure shows that the blade loading ranges from 0.84 to 0.96; such a small pressure span in the newly designed turbine is expected since it is designed to operate in such a small pressure ratio. In the region close to the hub (5% span), the flow separation can be clearly seen at the suction surface (around 20% chord) as indicated by sudden increment in the blade loading. This condition is best visualized by plotting the relative velocity on the meridional plane as shown in **Figures 23.a** to **23.c**. From these figures it can be seen that the separation only occurs at the suction surface of the blade (green circle) while on the pressure surface and at 50% pitch such a trend does not occur. A possible explanation for such behaviour at the hub of the turbine could be the sharp turning in the meridional direction; such a trend was also reported by Palfreyman and Martinez-Botas [10].

6 CONCLUSION

This paper has presented the design process of a high performance low pressure turbine energy recovery system for a turbocompounding unit of a downsized gasoline engine. The turbine design was motivated due to the improvement achieved in 1-D Ricardo Wave dynamic code. The simulation results have shown that an improvement in *BSFC* and *BMEP* of as much as 3 % can be achieved.

The conventional turbine design procedure can be applied to design the low pressure turbine and was proven numerically to give a high performance. The design procedure produced several possible turbine configurations. By using the design evaluation, it was found that the optimum blade number for the turbine rotor should be 9. The exit flow angle at the exit was set at -45˚ which resulted in a good compromise between the high aerodynamic performance and the manufacturability that required for the turbine. In addition to this the new turbine rotor design has a lower than usual exit-to-inlet area ratio, A_4/A_3 whereas a conventional turbine A_4/A_3 value is above than 0.8.

The CFD analysis has predicted very encouraging results. The predicted results show that the low pressure mixed-flow turbine achieved the maximum total-to-static efficiency of $\approx 76\%$ at a velocity ratio $VR \approx 0.7$. Also, the numerical CFD results prove that the turbine can achieve high performance for the pressure range going from 1.04 to 1.3 bar; outside this range the turbine performance was found to drop substantially.

Finally, a refined single passage CFD mesh was used to investigate the rotor flow field behaviour; the tip leakage and the passage loss could then be evaluated. A significant entropy generation occurs at the tip. However, the main turbine loss is the passage loss since the area of the main passage is much bigger than the tip clearance area and so is the entropy generated.

ACKNOWLEDGMENTS

The authors would like to acknowledge Ricardo plc, CPT , Ford UK, Valeo, and Ealabc. This consortium along with Imperial College is part of the Hyboost project, a funded program by TSB (Technical Strategical Board) whose support and encouragement is gratefully acknowledged.

The authors would also like to thank Universiti Teknologi MARA (UiTM) and Universiti Teknologi Malaysia (UTM) for their financial funding for the first and the second author.

REFERENCES

[1] Fraser, N., Blaxill, H., Lumsden, G., and Bassett, M., "Challenges for Increased Efficiency Through Gasoline Engine Downsizing," *SAE World Congress & Exhibition*, SAE International, New York, 2009.

[2] Hopmann, U. and Algrain, M. C., "Diesel Engine Electric Turbo Compound Technology," *Future Transportation Technology Conference & Exhibition*, SAE International, Warrendale, USA, 2003.

[3] Millo, F., Mallamo, F., Pautasso, E., and Mego, G. G., "The Potential of Electric Exhaust Gas Turbocharging for HD Diesel Engines," *SAE 2006 World Congress & Exhibition*, SAE International, Warrendale, USA, 2006.

[4] Kapich, D., "Turbo-Hydraulic Engine Exhaust Power Recovery System," *SAE Powertrain & Fluid Systems Conference & Exhibition*, San Diego, USA, 2002.

[5] Thompson, I. G. M., Spence, S. W., McCartan, C. D., and Talbot-Weiss, J. M. H., "Design, validation, and performance result of a turbocharged turbogenerating biogas engine model," *9th International Conference on Turbochargers and Turbocharging*, Charlesworth Group, Wakerfeild, London, UK, 2010, pp. 11-22.

[6] Wei, W., Zhuge, W., Zhang, Y., and He, Y., "Comparative Study on Electric Turbo-Compunding Systems for gasoline Engine Exhaust Energy Recovery," *ASME Turbo Expo 2010: Power for Land, Sea and Air*, ASME, Glasgow, Scotland, 2010.

[7] Zhuge, W., Zhang, Y., Zheng, X., Yang, M., and He, Y., "Development of an advanced turbocharger simulation method for cycle simulation of turbocharged internal combustion engines," *Proceedings of the Institution of Mechanical Engineers, Part D: Journal of Automobile Engineering*, Vol. 223, No. 5, 2009, pp. 661-672.

[8] Abidat, M., Hachemi, M., Hamidou, M. K., and Baines, N. C., "Prediction of the steady and non-steady flow performance of a highly loaded mixed flow turbine," *Proceedings of the Institution of Mechanical Engineers, Part A: Journal of Power and Energy*, Vol. 212, No. 3 A3, 1998, pp. 173-184.

[9] Bin Mamat, A. M. I. and Martinez-Botas, R., "Mean Line Flow Model of Steady and Pulsating Flow Of a Mixed-Flow Turbine Turbocharger," *ASME TURBO Expo 2010: Power for Land, Sea and Air (GT2010)*, Glasgow, 2010.

[10] Palfreyman, D. and Martinez-Botas, R., "Numerical Study of the Internal Flow Filed Characteristics in Mixed Flow Turbines," *ASME TURBO EXPO 2002*, ASME, Amsterdam, Netherlands, 2002.

[11] Abidat, M., Chen, H., Baines, N. C., and Firth, M. R., "Design of a highly loaded mixed flow turbine," *Proceedings of the Institution of Mechanical Engineers, Part A: Journal of Power and Energy*, Vol. 206, No. 2, 1992, pp. 95-107.

[12] Rajoo, S. and Martinez-Botas, R., "Mixed flow turbine research: A review," *Journal of Turbomachinery*, Vol. 130, No. 4, 2008.

[13] Karamanis, N., Martinez-Botas, R. F., and Su, C. C., "Mixed flow turbines: Inlet and exit flow under steady and pulsating conditions," *Journal of Turbomachinery*, Vol. 123, No. 2, 2001, pp. 359-371.

[14] Whitfield, A. and Mohd Noor, A. B., "Design and performance of vaneless volutes for radial inflow turbines. Part 1: Non-dimensional conceptual design considerations," *Proceedings of the Institution of Mechanical Engineers, Part A: Journal of Power and Energy*, Vol. 208, No. 3, 1994, pp. 199-211.

[15] Denton, J. D., "Some Limitations of Turbocmachinery CFD," *ASME Turbo Expo 2010*, ASME, Glasgow, Scotland, 2010.

[16] Whitfield, A. and Baines, N. C., *Design of Radial Turbomachines*, Longman Group UK Limited, Essex, England, 1990.

[17] Chen, H. and Baines, N. C., "The Aerodynamic Loading of Radial and Mixed-Flow Turbines," *International Jurnal of Mechanical Science,* Vol. 36, No. 1, 1993, pp. 63-79.

[18] Whitfield, A., Doyle, M. D. C., and Firth, M. R., "Design and performance of a high-pressure ratio turbocharger compressor Part 1: Design considerations," *Proceedings of the Institution of Mechanical Engineers, Part A: Journal of Power and Energy*, Vol. 207, No. 2, 1993, pp. 125-131.

[19] Copeland, C. D., Newton, P., Martinez-Botas, R., and Seiler, M., "The Effect of Unequal Admission on the Performance and Loss Generation in a Double-Entry Turbocharger Turbine," *ASME Turbo Expo 2010: Power for Land, Sea and Air (GT2010)*, ASME, Glasgow, Scotland, 2010.

[20] Simpson, A. T., Spence, S. W. T., and Watterson, J. K., "A comparison of the flow structures and losses within vaned and vaneless stators for radial turbines," *Journal of Turbomachinery*, Vol. 131, No. 3, 2009, pp. 031010.

[21] Karamanis, N., Palfreyman, D., Arcoumanis, C., and Martinez-Botas, R. F., "Steady and unsteady velocity measurements in a small turbocharger turbine with computational validation," *Journal of Physics: Series*, Vol. 45, No. 1, 2006, pp. 1.

[22] Palfreyman, D. and Martinez-Botas, R. F., "The pulsating flow field in a mixed flow turbocharger turbine: AN experimental and computational study," *2004 ASME Turbo Expo, June 14, 2004 - June 17, 2004*, Vol. 5 A, American Society of Mechanical Engineers, Vienna, Austria, 2004, pp. 697-708.

[23] Moore, J. and Moore, J. G., "Entropy Production Rates from Viscous Flow Calculations: Part 1- A Turbulent Boundary Layer Flow," The American Society of Mechanical Engineers (ASME), 83-GT-70, New York, U.S.A, Apr. 1983.

[24] Rohlik, H. E., "Analytical Determination of Radial Inflow Turbine Design Geometry for Maximum Efficiency," National Aeronautics and Space Administration, NASA TN D-4384, Washington, D.C United States of America, Feb. 1968.